

Spin-dependent electron transmission model for chiral molecules in mesoscopic devicesXu Yang,^{*} Caspar H. van der Wal, and Bart J. van Wees*Zernike Institute for Advanced Materials, University of Groningen, NL-9747AG Groningen, The Netherlands* (Received 5 October 2018; revised manuscript received 21 December 2018; published 18 January 2019)

Various device-based experiments have indicated that electron transfer in certain chiral molecules may be spin dependent, a phenomenon known as the chiral induced spin selectivity (CISS) effect. However, due to the complexity of these devices and a lack of theoretical understanding, it is not always clear to what extent the chiral character of the molecules actually contributes to the magnetic-field-dependent signals in these experiments. To address this issue, we report here an electron transmission model that evaluates the role of the CISS effect in two-terminal and multiterminal linear-regime electron transport experiments. Our model reveals that for the CISS effect, the chirality-dependent spin transmission is accompanied by a spin-flip electron reflection process. Furthermore, we show that more than two terminals are required in order to probe the CISS effect in the linear regime. In addition, we propose two types of multiterminal nonlocal transport measurements that can distinguish the CISS effect from other magnetic-field-dependent signals. Our model provides an effective tool to review and design CISS-related transport experiments, and to enlighten the mechanism of the CISS effect itself.

DOI: [10.1103/PhysRevB.99.024418](https://doi.org/10.1103/PhysRevB.99.024418)**I. INTRODUCTION**

Developments in the semiconductor industry have allowed integrated circuits to rapidly shrink in size, reaching the limit of conventional silicon-based electronics. One idea to go beyond this limit is to use the spin degree of freedom of electrons to store and process information (spintronics) [1]. A spintronic device usually contains two important components: a spin injector and a spin detector, through which electrical or optical signals and spin signals can be interconverted. Conventionally, this conversion is done with bulky solid-state materials, but the recently discovered chiral induced spin selectivity (CISS) effect suggests that certain chiral molecules or their assemblies are capable of generating spin signals as well. This effect describes that electrons acquire a spin polarization while being transmitted through certain chiral (helical) molecules. Notably, experimental observations of the CISS effect suggest its existence, but complete theoretical insight in its origin is still lacking [2,3]. The CISS effect is thus not only relevant for spintronic applications, but also fundamentally interesting.

The CISS effect has been experimentally reported in chiral (helical) systems ranging from large biological units such as dsDNA [4,5] to small molecules such as helicenenes [6,7]. Typically, these experiments can be categorized into either electron photoemission experiments [4,7–13] or magnetotransport measurements [5,6,14–20]. The latter, in particular, are usually based on solid-state devices and are of great importance to the goal of realizing chiral-molecule-based spintronics. Important to realize, in such devices, the CISS-related signals may often be overshadowed by other spurious signals that arise from magnetic components of the devices. Therefore, it is essential to understand the exact role of chiral molecules

in these devices and to distinguish between the CISS-related signals and other magnetic-field-dependent signals. However, this has not been addressed, and an effective tool to perform such analyses is still missing.

We provide here a model that is based on the Landauer-Büttiker-type of analysis of linear-regime electron transmission and reflection. Unlike other theoretical works [21–29], our model is derived from symmetry theorems that hold for electrical conduction in general and does not require any assumptions about the CISS effect on a molecular level. With this model, we quantitatively demonstrate how the CISS effect leads to spin injection and detection in linear-regime devices, and analyze whether typical two-terminal and four-terminal measurements are capable of detecting the CISS effect in the linear regime.

II. MODEL

We consider a solid-state device as a linear-regime circuit segment whose constituents are described by the following set of rules:

(i) A *contact* [pictured as a wavy line segment perpendicular to the current flow (see, e.g., Fig. 1)] is described as an electron reservoir with a well-defined chemical potential μ , which determines the energy of the electrons that leave the reservoir. A reservoir absorbs all incoming electrons regardless of its energy or spin.

(ii) A *node* (pictured as a circle, see later figures for four-terminal geometries) is a circuit constituent where chemical potentials for charge and spin are defined. It is described by two chemical potentials μ_{\rightarrow} and μ_{\leftarrow} , one for each spin species with the arrows indicating the spin orientations. At a node a spin accumulation μ_s is defined ($\mu_s = \mu_{\rightarrow} - \mu_{\leftarrow}$). Inside a node the momentum of electrons is randomized, while the spin is preserved. The function and importance of the node will be further addressed in the discussion section.

^{*}xu.yang@rug.nl

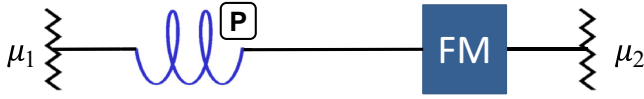


FIG. 1. A two-terminal circuit segment with a P -type CISS molecule and a ferromagnet between contacts 1 and 2 (with chemical potentials μ_1 and μ_2). The notion P type represents the chirality of the molecule and indicates that it allows higher transmission for spins *parallel* to the electron momentum. (The opposite chirality allows higher transmission for spins *antiparallel* to the electron momentum, and is denoted as AP type.) The ferromagnet (FM) is assumed to allow higher transmission of spins parallel to its magnetization direction, which can be controlled to be either parallel or antiparallel to the electron transport direction.

(iii) A *CISS molecule* [pictured as a helix, color coded and labeled for its chirality (see, e.g., Fig. 1)], a *ferromagnet* [a filled square (see, e.g., Fig. 1)], and a *nonmagnetic barrier* [a shaded rectangle (see, e.g., Fig. 2)] are viewed as two-terminal circuit constituents with energy-conserving electron transmissions and reflections. Each of them is described by a set of (possibly spin-dependent) transmission and reflection probabilities;

(iv) The above constituents are connected to each other via *transport channels* [pictured as line segments along the current flow (see, e.g., Fig. 1)], in which both the momentum and the spin of electrons are preserved.

Before proceeding with introducing the model, we would like to highlight the important role of dephasing in the

	Transmission	Reflection
General form	$\mathbb{T} = \begin{pmatrix} t_{\rightarrow\rightarrow} & t_{\leftarrow\rightarrow} \\ t_{\rightarrow\leftarrow} & t_{\leftarrow\leftarrow} \end{pmatrix}$	$\mathbb{R} = \begin{pmatrix} r_{\rightarrow\rightarrow} & r_{\leftarrow\rightarrow} \\ r_{\rightarrow\leftarrow} & r_{\leftarrow\leftarrow} \end{pmatrix}$
Nonmagnetic barrier	$\mathbb{T}_B = \begin{pmatrix} t & 0 \\ 0 & t \end{pmatrix}$	$\mathbb{R}_B = \begin{pmatrix} 1-t & 0 \\ 0 & 1-t \end{pmatrix}$
Ferromagnet	$\mathbb{T}_{\text{FM}} = \begin{pmatrix} \frac{1+P_{\text{FM}}}{2} & 0 \\ 0 & \frac{1-P_{\text{FM}}}{2} \end{pmatrix}$	$\mathbb{R}_{\text{FM}} = \begin{pmatrix} \frac{1-P_{\text{FM}}}{2} & 0 \\ 0 & \frac{1+P_{\text{FM}}}{2} \end{pmatrix}$
P -type ideal CISS molecule	$\mathbb{T}_{0,R}^P = \begin{pmatrix} 1 & 0 \\ 0 & 0 \end{pmatrix}$ $\mathbb{T}_{0,L}^P = \begin{pmatrix} 0 & 0 \\ 0 & 1 \end{pmatrix}$	$\mathbb{R}_{0,R}^P = \begin{pmatrix} 0 & 1 \\ 0 & 0 \end{pmatrix}$ $\mathbb{R}_{0,L}^P = \begin{pmatrix} 0 & 0 \\ 1 & 0 \end{pmatrix}$
AP -type ideal CISS molecule	$\mathbb{T}_{0,R}^{AP} = \mathbb{T}_{0,L}^P$ $\mathbb{T}_{0,L}^{AP} = \mathbb{T}_{0,R}^P$	$\mathbb{R}_{0,R}^{AP} = \mathbb{R}_{0,L}^P$ $\mathbb{R}_{0,L}^{AP} = \mathbb{R}_{0,R}^P$

FIG. 2. Transmission and reflection matrices (\mathbb{T} and \mathbb{R}) for a nonmagnetic barrier (subscript B , here we use the term *barrier*, but it refers to any circuit constituent with spin-independent electron transmission and reflection), a ferromagnet (subscript FM), and ideal P -type (superscript P) and AP -type (superscript AP) CISS molecules. For the CISS molecules the subscripts R (right) and L (left) denote the direction of the incoming electron flow, and the indicator 0 in the subscripts means these matrices are for an ideal case where all the matrix elements are either 1 or 0. The matrices for AP -type molecules are derived from those for P -type molecules under the assumption that opposite chiral enantiomers are exact mirror images of each other, and therefore select opposite spins with equal probability. Each matrix element represents the probability of a spin-dependent transmission or reflection, with the column/row position indicating the corresponding spin orientations before/after the transmission or reflection (see general form in the top row).

generation of the CISS effect. In a fully phase-coherent two-terminal electron transport system, time-reversal symmetry prohibits the production of spin polarization by a charge current [30]. Consequently, a CISS molecule requires the presence of dephasing in order to exhibit a CISS-type spin-polarizing behavior. The necessity of dephasing has already been addressed by other theoretical works [31–33]. Here, we emphasize that the Landauer-Buttiker type of analysis, on which our model is based, does not require phase coherence [34,35]. Moreover, dephasing can be naturally provided by inelastic processes such as electron-phonon interactions under experimental conditions. Therefore, it is reasonable to assume that a CISS molecule is able to generate a spin polarization in a linear-regime circuit segment, and our discussions focus on whether this spin polarization can be detected as a charge signal.

In the following part of this paper, we first derive a key transport property of CISS molecules and then introduce a matrix formalism to quantitatively describe linear-regime transport devices. Later, in the discussion section, we provide analyses for a few experimental circuit geometries.

A. Reciprocity and spin-flip reflection by chiral molecules

In order to characterize the CISS effect without having to understand it on a molecular level, we look at universal rules that apply to any conductor in the linear regime, namely, the law of charge conservation and the reciprocity theorem.

The reciprocity theorem states that for a multiterminal circuit segment in the linear regime, the measured conductance remains invariant when an exchange of voltage and current contacts is accompanied by a reversal of magnetic field H and magnetization M (of all magnetic components) [36,37]. Mathematically, we write

$$G_{ij,mn}(H, M) = G_{mn,ij}(-H, -M), \quad (1)$$

where $G_{ij,mn}$ is the four-terminal conductance measured using current contacts i and j and voltage contacts m and n . In two-terminal measurements, this theorem reduces to

$$G_{ij}(H, M) = G_{ij}(-H, -M), \quad (2)$$

meaning that the two-terminal conductance remains constant under magnetic field and magnetization reversal. This theorem emphasizes the universal symmetry independent of the microscopic nature of the transport between electrical contacts. It is valid for any linear-regime circuit segment regardless of the number of contacts, or the presence of inelastic scattering events [37].

By applying the reciprocity theorem to a circuit segment containing CISS molecules, one can derive a special transport property of these molecules. For example, in the two-terminal circuit segment shown in Fig. 1, the reciprocity theorem requires that the two-terminal conductance remains unchanged when the magnetization direction of the ferromagnet is reversed. Since the two-terminal conductance is proportional to the transmission probability between the two contacts (Landauer-Büttiker) [35], this requirement translates to

$$T_{21}(\Rightarrow) = T_{21}(\Leftarrow), \quad (3)$$

where T_{21} describes the transmission probability of electrons injected from contact 1 to reach contact 2, and \Rightarrow and \Leftarrow indicate the magnetization directions of the ferromagnet. This requirement gives rise to a necessary spin-flip process associated with the CISS molecule, as described below.

For ease of illustration, we assume an ideal case where both the ferromagnet and the CISS molecule allow a 100% transmission of the favored spin and a 100% reflection of the other (the general validity of the conclusions is addressed in Appendix A). We consider electron transport from contact 1 to contact 2 (see Fig. 1) and compare the two transmission probabilities $T_{21}(\Rightarrow)$ and $T_{21}(\Leftarrow)$. For $T_{21}(\Rightarrow)$, the P -type CISS molecule (favors spin parallel to electron momentum, see figure caption) allows the transmission of spin-right electrons, while it reflects spin-left electrons back to contact 1. At the same time, the ferromagnet is magnetized to also only allow the transmission of spin-right electrons. Therefore, all spin-right (and none of the spin-left) electrons can be transmitted to contact 2, giving $T_{21}(\Rightarrow) = 0.5$. As for $T_{21}(\Leftarrow)$, while the P -type CISS molecule still allows the transmission of spin-right electrons, the ferromagnet no longer does. It reflects the spin-right electrons towards the CISS molecule with their momentum antiparallel to their spin. As a result, these electrons are reflected by the CISS molecule and are confined between the CISS molecule and the ferromagnet. This situation gives $T_{21}(\Leftarrow) = 0$, which is not consistent with Eq. (3). In order to satisfy Eq. (3), i.e., to have $T_{21}(\Leftarrow) = 0.5$, a spin-flip process has to take place for the spin-right electrons, so that they can be transmitted to contact 2 through the ferromagnet. Such a process does not exist for the ideal and exactly aligned ferromagnet. Therefore, a spin-flip electron reflection process must exist for the CISS molecule. Further analysis (see Appendix A) shows that such a spin-flip reflection process completely meets the broader restrictions from Eq. (2). In addition, the conclusion that a spin-flip reflection process must exist is valid for general cases where the ferromagnet and the CISS molecule are not ideal (see Appendix A).

In these derivations, the only assumption regarding the CISS molecule is that it allows higher transmission of one spin than the other, which is a conceptual description of the CISS effect itself. Therefore, the spin-flip reflection process has to be regarded as an inherent property of the CISS effect in a linear-regime transport system, and this is guaranteed by the universal symmetry theorems of electrical conduction [36,37].

B. Matrix formalism and barrier-CISS center-barrier (BCB) model for CISS molecules

We use matrices to quantitatively describe the spin-dependent transmission and reflection probabilities of CISS molecules and other circuit constituents, as shown in Fig. 2. At the top of the figure, the general form of these matrices is introduced. Matrix element $t_{\alpha\beta}$ (or $r_{\alpha\beta}$), where α and β is either *left* (\Leftarrow) or *right* (\Rightarrow), represents the probability of a spin- α electron being transmitted (or reflected) as a spin- β electron, and $\alpha \neq \beta$ indicates a spin-flip process. Here, $0 \leq t_{\alpha\beta}, r_{\alpha\beta} \leq 1$, and the spin orientations are chosen to be either parallel or antiparallel to the electron momentum in later discussions. Next, the transmission and reflection

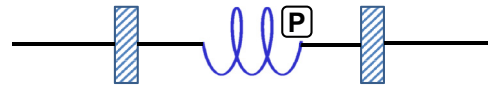


FIG. 3. A generalized *barrier-CISS center-barrier (BCB)* model for P -type CISS molecules. The ideal, 100%-spin-selective CISS center in the middle introduces the directional spin transmission in a CISS molecule, while the two identical nonmagnetic barriers (with transmission probability t) contribute the nonideal electron transmission and reflection behavior. The overall transmission and reflection matrices of the entire BCB module are fully determined by t and have all elements taking finite values between 0 and 1.

matrices of a nonmagnetic barrier are given. These matrices are spin independent and are fully determined by a transmission probability t ($0 \leq t \leq 1$), which depends on the material and dimensions of the barrier. Here, we use the term *barrier*, but it refers to any circuit constituent with spin-independent electron transmission and reflection. In the third row, we show the transmission and reflection matrices of a ferromagnet. These matrices are spin dependent, and are determined by the polarization P_{FM} ($0 < |P_{\text{FM}}| \leq 1$) of the ferromagnet. Finally, for P -type and AP -type CISS molecules, we show here an ideal case where all the matrix elements are either 1 or 0. The nonzero off-diagonal terms in the reflection matrices represent the characteristic spin-flip reflections. These ideal CISS molecules are later referred to as CISS centers, and will be generalized for more realistic situations.

In accordance with the matrix formalism, we use column vector $\boldsymbol{\mu} = \begin{pmatrix} \mu_{\rightarrow} \\ \mu_{\leftarrow} \end{pmatrix}$ to describe chemical potentials, and column vector $\boldsymbol{I} = \begin{pmatrix} I_{\rightarrow} \\ I_{\leftarrow} \end{pmatrix}$ to describe currents, where each vector element describes the contribution from one spin component (indicated by arrow).

A nonideal CISS molecule with C_2 symmetry (twofold rotational symmetry with an axis perpendicular to the electron transport path) can be modeled as a linear arrangement of two identical barriers sandwiching an ideal CISS center, as shown in Fig. 3 (only the P type is shown). In this barrier-CISS center-barrier (BCB) model we consider that all spin-dependent linear-regime transport properties of a CISS molecule exclusively originate from an ideal CISS center inside the molecule, and the overall spin dependency is limited by the multiple spin-independent transmissions and reflections at other parts (nonmagnetic barriers) of the molecule. Therefore, the barrier transmission probability t ($0 < t \leq 1$) fully determines the transmission and reflection matrices of the entire BCB molecule, and consequently determines the spin-related properties of the molecule. The use of an identical barrier on each side of the CISS center is to address the C_2 symmetry. However, we stress that not all CISS molecules have this symmetry, and the BCB model is still a simplified picture. The model can be further generalized by removing the restriction of the CISS center being ideal, and this case is discussed in Appendix C. Despite being a simplified picture, the BCB model captures all qualitative behaviors of a nonideal CISS molecule, and at the same time keeps quantitative analyses simple. Therefore, we further only discuss the case of BCB molecules, instead of the more generalized CISS molecules.

III. DISCUSSIONS

In this section, we use different approaches to separately analyze two-terminal and multiterminal circuit geometries. For two-terminal geometries, we evaluate the conductance of the circuit segment by calculating the electron transmission probability T_{21} between the two contacts. In contrast, for multiterminal geometries, we take a circuit-theory approach to evaluate the spin accumulation μ_s at the nodes.

A major difference between the two approaches is the inclusion of nodes in multiterminal geometries. In our description, a node is the only location where spin accumulation can be defined. It can be experimentally realized with a diffusive electron transport channel segment that is much shorter (along the electron transport direction) than the spin-diffusion length λ_s of the channel material. Due to its diffusive nature, a node emits electrons to all directions, so it can be considered as a source of electron backscattering. Notably, adding a node to a near-ideal electron transport channel (with transmission probability close to 1) significantly alters its electron transmission probability. Nonetheless, this does not affect the validity of our approach because we only address nonideal circuit segments where electron backscattering (reflection) already exists due to other circuit constituents (CISS molecules, ferromagnets, or nonmagnetic barriers). Note that even when we discuss the use of ideal CISS molecules or ideal ferromagnets, the entire circuit segment is nonideal due to the reflection of the rejected spins.

In the following discussion, we consider only the P -type BCB molecule, and we use expressions $\mathbb{T}_{R,L}^P$ and $\mathbb{R}_{R,L}^P$ to describe transmission and reflection matrices of the entire BCB module, where the subscripts consider electron flow directions. The derivations of these matrices can be found in Appendix B.

A. Two-terminal geometries

We discuss here two geometries that are relevant for two-terminal magnetoresistance measurements [38]. The first is an FM-BCB geometry, as shown in Fig. 4. It simulates a common type of experiment where a layer of chiral molecules is sandwiched between a ferromagnetic layer and a normal metal contact. The other side of the ferromagnetic layer is also connected to a normal metal contact (experimentally this may be a wire that connects the sample with the measurement instrument). Due to the spin-dependent transmission of the chiral molecules and the ferromagnet, one might expect a change of the two-terminal conductance once the magnetization of the ferromagnet is reversed. However, this change is not allowed by the reciprocity theorem [Eq. (2)], which can be confirmed with our model, as explained below.

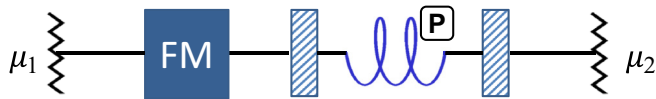


FIG. 4. An FM-BCB geometry where a ferromagnet and a BCB molecule are connected in series in a two-terminal circuit segment. The magnetization reversal of the ferromagnet does not change the two-terminal conductance.

In order to illustrate this, we calculate the electron transmission probabilities between the two contacts for opposite ferromagnet magnetization directions $T_{21}^{\text{FM-BCB}}(\Rightarrow)$ and $T_{21}^{\text{FM-BCB}}(\Leftarrow)$, where the arrows indicate the magnetization directions.

For the magnetization direction to the right (\Rightarrow), we first derive the transmission and reflection matrices with the combined contribution from the ferromagnet and the BCB molecule

$$\begin{aligned} \mathbb{T}_{21}^{\text{FM-BCB}}(\Rightarrow) &= \mathbb{T}_R^P \cdot (\mathbb{I} + \mathbb{R}_{\text{FM}}(\Rightarrow) \cdot \mathbb{R}_R^P + (\mathbb{R}_{\text{FM}}(\Rightarrow) \cdot \mathbb{R}_R^P)^2 \\ &\quad + (\mathbb{R}_{\text{FM}}(\Rightarrow) \cdot \mathbb{R}_R^P)^3 + \dots) \cdot \mathbb{T}_{\text{FM}}(\Rightarrow) \\ &= \mathbb{T}_R^P \cdot (\mathbb{I} - \mathbb{R}_{\text{FM}}(\Rightarrow) \cdot \mathbb{R}_R^P)^{-1} \cdot \mathbb{T}_{\text{FM}}(\Rightarrow), \end{aligned} \quad (4a)$$

$$\begin{aligned} \mathbb{R}_{11}^{\text{FM-BCB}}(\Rightarrow) &= \mathbb{R}_{\text{FM}}(\Rightarrow) + \mathbb{T}_{\text{FM}}(\Rightarrow) \cdot (\mathbb{I} - \mathbb{R}_R^P \cdot \mathbb{R}_{\text{FM}}(\Rightarrow))^{-1} \\ &\quad \cdot \mathbb{R}_R^P \cdot \mathbb{T}_{\text{FM}}(\Rightarrow), \end{aligned} \quad (4b)$$

where the $\mathbb{I} = \begin{pmatrix} 1 & 0 \\ 0 & 1 \end{pmatrix}$ is the identity matrix. The addition of the multiple reflection terms is due to the multiple reflections between the ferromagnet and the BCB molecule. Next, we include the contribution from the contacts and derive the transmission and reflection probabilities accounting for both spins

$$T_{21}^{\text{FM-BCB}}(\Rightarrow) = (1, 1) \mathbb{T}_{21}^{\text{FM-BCB}}(\Rightarrow) \begin{pmatrix} 1/2 \\ 1/2 \end{pmatrix}, \quad (5a)$$

$$R_{11}^{\text{FM-BCB}}(\Rightarrow) = (1, 1) \mathbb{R}_{11}^{\text{FM-BCB}}(\Rightarrow) \begin{pmatrix} 1/2 \\ 1/2 \end{pmatrix}, \quad (5b)$$

where the column vector $\begin{pmatrix} 1/2 \\ 1/2 \end{pmatrix}$ describes the normalized input current from contact 1 with equal spin-right and spin-left contributions, and the row vector $(1, 1)$ is an operator that describes the absorption of both spins into contact 2 (calculates the sum of the two spin components).

For the opposite magnetization direction (\Leftarrow), we change the magnetization-dependent terms in Eqs. (4) and (5) accordingly. Detailed calculations (see Appendix B) prove

$$T_{21}^{\text{FM-BCB}}(\Rightarrow) \equiv T_{21}^{\text{FM-BCB}}(\Leftarrow) \quad (6)$$

for all BCB transmission probabilities t and all ferromagnet polarizations P_{FM} . Therefore, it is not possible to detect any variation of two-terminal conductance in this geometry by switching the magnetization direction of the ferromagnet. In Appendix B we show that it is also not possible to detect any variation of two-terminal conductance by reversing the current, and that the above conclusions also hold for the more generalized CISS model (Appendix C). These conclusions also agree with earlier reports on general voltage-based detections of current-induced spin signals [39].

The second geometry, as shown in Fig. 5, contains two ferromagnets, and is similar to a spin valve. In a conventional spin valve (a nonmagnetic barrier sandwiched between two ferromagnets), the magnetization reversal of one ferromagnet leads to a change of the two-terminal conductance [38] (this does not violate the reciprocity theorem since switching one ferromagnet does not reverse all magnetizations of the entire circuit segment), whereas in the geometry shown in Fig. 5,

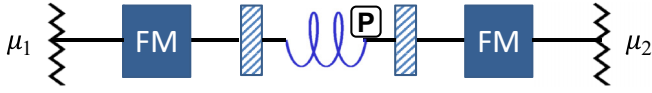


FIG. 5. A spin-valve geometry with a BCB molecule placed in-between two ferromagnets. Unlike a conventional spin valve, here the magnetization reversal of one ferromagnet does not change the two-terminal conductance due to the presence of the BCB molecule.

this change does not happen due to the presence of spin-flip electron reflections in the BCB molecule. (See Appendix B for more details.) As a result, this geometry is not able to quantitatively measure the CISS effect. We emphasize that here the absence of the spin-valve behavior is unique for the BCB model, which contains an ideal CISS center. In Appendix C we show that a further-generalized CISS model regains the spin-valve behavior. Nevertheless, one cannot experimentally distinguish whether the regained spin-valve behavior originates from the CISS molecule or a normal nonmagnetic barrier, and therefore cannot draw any conclusion about the CISS effect. In general, it is not possible to measure the CISS effect in the linear regime using two-terminal experiments.

B. Four-terminal geometries and experimental designs

Four-terminal measurements allow one to completely separate spin-related signals from charge-related signals, and therefore allow the detection of spin accumulations created by the CISS effect [40]. Here, we analyze two geometries that are relevant for such measurements. In the first geometry, we use a node connected to BCB molecules to illustrate how spin injection and detection can occur without using magnetic materials (Fig. 6). In the second geometry, we use two nodes to decouple a BCB molecule from electrical contacts and illustrate the spin-charge conversion property of the molecule (Fig. 7). In addition, we propose device designs that resemble these two geometries and discuss possible experimental outcomes (Fig. 8).

Figure 6(a) shows a geometry where a node is connected to four contacts. Two of the contacts contain BCB molecules, and the other two contain nonmagnetic (tunnel) barriers. We consider an experiment where contacts 1 and 2 are used for current injection and contacts 3 and 4 are used for voltage detection. In terms of spin injection, we first assume that the voltage contacts 3 and 4 are weakly coupled to the node, and do not contribute to the spin accumulation in the node. This means that the chemical potentials of contacts 1 and 2 fully determine the spin-dependent chemical potential (column vector) of the node $\mu_{\text{node}} = \begin{pmatrix} \mu_{\text{node}\rightarrow} \\ \mu_{\text{node}\leftarrow} \end{pmatrix}$. We also assume $\mu_2 = 0$ for convenience since only the chemical potential difference between the two contacts is relevant. Under these assumptions, the node receives electrons only from contact 1, but emits electrons to both contacts 1 and 2. Therefore, the incoming current (column vector) into the node is

$$\mathbf{I}_{\text{in}} = \frac{G}{e} \mathbb{T}_R^P \mu_1 \begin{pmatrix} 1 \\ 1 \end{pmatrix}, \quad (7)$$

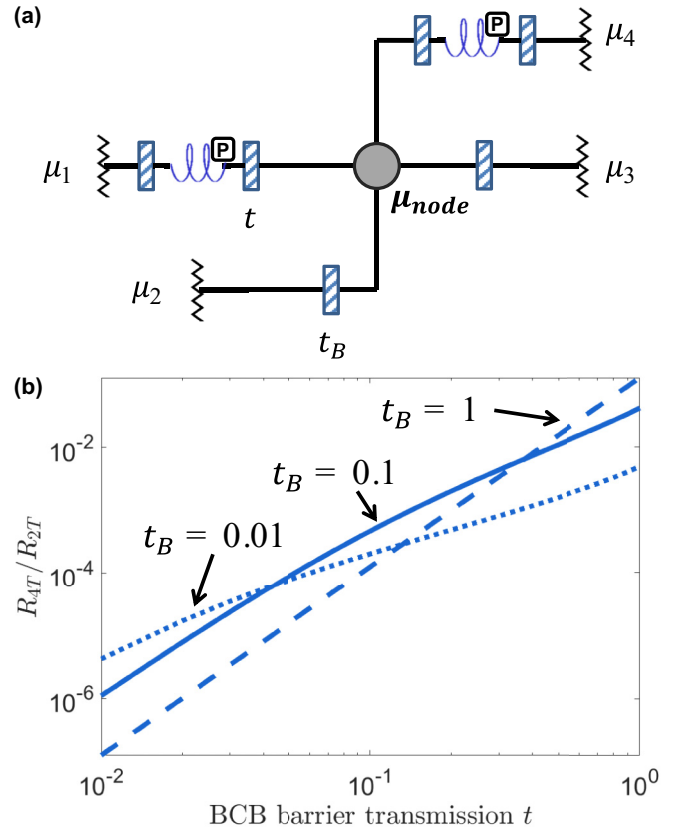


FIG. 6. (a) A four-terminal geometry that includes a node. Two of the contacts contain BCB molecules, and the other two are coupled to the node via tunnel barriers (with transmission probability t_B). The node is characterized by a spin-dependent chemical potential vector $\mu_{\text{node}} = \begin{pmatrix} \mu_{\text{node}\rightarrow} \\ \mu_{\text{node}\leftarrow} \end{pmatrix}$, and each of the four contacts is characterized by a spin-independent chemical potential μ_i , with $i = 1, 2, 3, 4$. (b) Calculated ratio between four-terminal and two-terminal resistances for this geometry, plotted as a function of t (transmission probability of the barriers in BCB molecules) for three t_B (transmission probability of the barriers at the contacts) values.

and the outgoing current (column vector) from the node is

$$\mathbf{I}_{\text{out}} = \frac{G}{e} ((\mathbb{I} - \mathbb{R}_L^P) + (1 - r_B)\mathbb{I}) \mu_{\text{node}}, \quad (8)$$

where $G = Ne^2/h$ is the N -channel, one-spin conductance of the channels connecting the node to each of the contacts, and r_B ($0 \leq r_B \leq 1$) is the reflection probability of the tunnel barrier between the node and contact 2 (different from the barriers in BCB molecules). Due to the spin-preserving nature of the node, at steady state the incoming current is equal to the outgoing current (for both spin components), or $\mathbf{I}_{\text{in}} = \mathbf{I}_{\text{out}}$. From this relation we derive

$$\mu_{\text{node}} = ((1 + t_B)\mathbb{I} - \mathbb{R}_L^P)^{-1} \mathbb{T}_R^P \mu_1 \begin{pmatrix} 1 \\ 1 \end{pmatrix}, \quad (9)$$

where $t_B = 1 - r_B$ is the transmission probability of the tunnel barrier. Next, we derive the spin accumulation in the node

$$\mu_s = \mu_{\text{node}\rightarrow} - \mu_{\text{node}\leftarrow} = (1, -1) \mu_{\text{node}} = k_{inj} \mu_1, \quad (10)$$

where a row vector $(1, -1)$ is used as an operator to calculate the difference between the two spin chemical potentials, and

$$k_{inj} = (1, -1)((1 + t_B)\mathbb{I} - \mathbb{R}_L^P)^{-1} \mathbb{T}_R^P \begin{pmatrix} 1 \\ 1 \end{pmatrix}, \quad (11)$$

with $0 < k_{inj} \leq \frac{1}{4}$,

is the spin *injection coefficient* for these current contacts. This expression shows that the spin accumulation in the node depends linearly on the chemical potential difference between the current contacts, and the coefficient k_{inj} is determined by both the BCB molecule (with parameter t) and the tunnel barrier connected to contact 2 (with parameter t_B).

With regard to spin detection, we discuss whether the established spin accumulation μ_s in the node can lead to a chemical potential difference (and thus a charge voltage) between the weakly coupled voltage contacts 3 and 4. A contact cannot distinguish between the two spin components, therefore, only the charge current (sum of both spins, calculated by applying an operator $(1, 1)$ to a current column vector) is relevant. At steady state, there is no net charge current at any of the voltage contacts,

$$I_3 = \frac{G}{e}(1, 1) \left((1 - r_B)\mu_3 \begin{pmatrix} 1 \\ 1 \end{pmatrix} - t_B \mu_{\text{node}} \right) = 0, \quad (12a)$$

$$I_4 = \frac{G}{e}(1, 1) \left((\mathbb{I} - \mathbb{R}_L^P)\mu_4 \begin{pmatrix} 1 \\ 1 \end{pmatrix} - \mathbb{T}_R^P \mu_{\text{node}} \right) = 0, \quad (12b)$$

which gives

$$\mu_4 - \mu_3 = k_{\text{det}} \mu_s, \quad (13)$$

where

$$k_{\text{det}} = \frac{1}{2} \frac{(1, 1) \mathbb{T}_R^P \begin{pmatrix} 1 \\ -1 \end{pmatrix}}{(1, 1) \mathbb{T}_L^P \begin{pmatrix} 1 \\ 1 \end{pmatrix}}, \quad (14)$$

with $0 < k_{\text{det}} \leq \frac{1}{2}$,

is the spin *detection coefficient* for these voltage contacts. This expression shows that the chemical potential difference between the two voltage contacts depends linearly on the spin accumulation in the node, and the coefficient k_{det} is exclusively determined by the BCB molecule (with parameter t).

Combining Eqs. (10) and (13) we obtain

$$\frac{R_{4T}}{R_{2T}} = \frac{\mu_4 - \mu_3}{\mu_1 - \mu_2} = k_{inj} k_{\text{det}}, \quad (15)$$

where R_{4T} is the four-terminal resistance (measured using contacts 3 and 4 as voltage contacts, while using contacts 1 and 2 as current contacts), and R_{2T} is the two-terminal resistance (measured using contacts 1 and 2 as both voltage and current contacts). This ratio is determined by both the BCB molecule (with parameter t) and the tunnel barrier connected to contact 2 (with parameter t_B), and can be experimentally measured to quantitatively characterize the CISS effect.

As an example, for $t = t_B = 0.5$, we have $k_{inj} \approx 0.11$, $k_{\text{det}} \approx 0.17$, and $R_{4T}/R_{2T} \approx 0.02$. In Fig. 6(b) we plot

R_{4T}/R_{2T} as a function of t for three different t_B values. Similar plots for k_{inj} and k_{det} are shown in Appendix B.

The above results show that it is possible to inject and detect a spin accumulation in a node using only BCB molecules and nonmagnetic (tunnel) barriers, and these processes can be quantitatively described by the injection and detection coefficients. We stress that the signs of the injection and detection coefficients depend on the type (chirality) of the BCB molecule and the position of the molecule with respect to the contact. Switching the molecule from P type to AP type leads to a sign change of the injection or detection coefficient. The sign change also happens if the contact is connected to the opposite side of the BCB molecule. For example, in Fig. 6(a), contacts 1 and 4 are both connected to the node via P -type BCB molecules, but contact 1 is on the left-hand side of a molecule, while contact 4 is on the right-hand side. Electrons emitted from these two contacts travel in opposite directions through the (same type of) BCB molecules before arriving at the node. As a result, using contact 4 instead of contact 1 as a current contact leads to a sign change of k_{inj} . Similarly, using contact 1 instead of contact 4 as a voltage contact leads to a sign change of k_{det} . Experimentally, one can use three BCB contacts to observe this sign change: a fixed current contact (thus a fixed k_{inj}) in combination with two voltage contacts that use the same type of BCB molecule but are placed on opposite sides of a node (thus opposite signs for k_{det}). The voltages measured by the two voltage contacts (with respect to a common reference contact) will differ by sign. This can be experimentally measured as a signature of the CISS effect.

Figure 7 shows a geometry where a BCB molecule is between two nodes A and B , and is decoupled from the contacts. The nodes themselves are connected to contacts in a similar fashion as in the previous geometry. In node A , we consider a chemical potential vector μ_A and a spin accumulation μ_{sA} , which are fully determined by the current contacts 1 and 2. In node B , we consider weakly coupled voltage contacts 3 and 4, so that its chemical potential vector μ_B and its spin accumulation μ_{sB} , are fully determined by μ_A . At steady state, there is no net charge or spin current in node B , which leads to

$$\mu_B = (\mathbb{I} - \mathbb{R}_L^P)^{-1} \mathbb{T}_R^P \mu_A. \quad (16)$$

Note that here the matrices only refer to the molecule between the two nodes. For BCB molecules, this expression always gives $\mu_{sB} = 0$, but for a more generalized CISS molecule (as described in Appendix C), this expression can give $\mu_{sB} \neq 0$. This shows that a spin accumulation at one side of a CISS

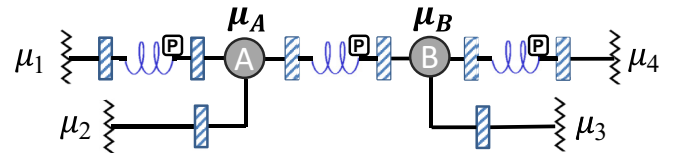


FIG. 7. A four-terminal geometry involving two nodes A and B , which are connected to each other via a BCB molecule. A spin accumulation difference between the two nodes results in a (charge) chemical potential difference between them, and vice versa.

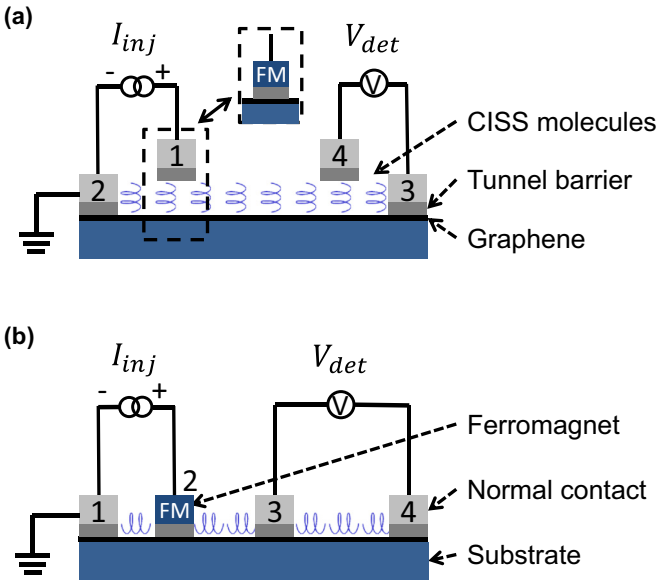


FIG. 8. Nonlocal device designs with CISS molecules adsorbed on graphene. (a) A device where electrons travel through CISS molecules. All contacts are nonmagnetic and are numbered in agreement with Fig. 6(a). A variation of this device can be achieved by replacing contact 1 with a ferromagnet (see inset). (b) A device where electrons travel in proximity to CISS molecules. A ferromagnetic contact 2 is used for spin injection, but one can also use only nonmagnetic contacts, as in Fig. 7.

molecule can generate a spin accumulation at the other side of the molecule. Most importantly, for both the BCB model and the more generalized model, Eq. (16) predicts that a spin accumulation difference across a CISS molecule creates a charge voltage across the molecule, and vice versa (spin-charge conversion via a CISS molecule). Mathematically written, the expression always provides $\mu_{nA} \neq \mu_{nB}$ when $\mu_{sA} \neq \mu_{sB}$, and $\mu_{sA} \neq \mu_{sB}$ when $\mu_{nA} \neq \mu_{nB}$, where μ_{nA} (or μ_{nB}) is the average chemical potential of the two spin components in node A (or in node B). A more detailed description of this geometry can be found in Appendix C.

Figure 8 shows two types of nonlocal devices that resemble the two geometries introduced above. We realize the node function with graphene, chosen for its long spin lifetime and long spin diffusion length [41]. The first type, as shown in Fig. 8(a), represents the geometry in Fig. 6(a), where spin injection and detection are both achieved using CISS molecules. A current I_{inj} is injected from contact 1 through CISS molecules into graphene, then driven out to a normal metal contact 2. This current induces a spin accumulation in the graphene layer underneath the current contacts, which then diffuses to the voltage contacts. The voltage contacts then pick up a charge voltage V_{det} in a similar fashion as explained in Fig. 6(a). With this, the nonlocal resistance can be determined $R_{nl} = V_{det}/I_{inj}$. Further, we can derive (see Appendix B for details)

$$R_{nl} = -k_{inj}k_{det}R_{inj}e^{-\frac{d}{\lambda_s}}, \quad (17)$$

where R_{inj} is the resistance measured between the current contacts 1 and 2, d is the distance between contacts 1 and 4,

and λ_s is the spin diffusion length of graphene. It is assumed here that the spacing between the current contacts (1 and 2) and the spacing between the voltage contacts (3 and 4) are both much smaller than λ_s . The minus sign comes from the fact that the injection and the detection contacts are on the same side of the graphene channel (both on top), unlike the example in Fig. 6(a) (one on the left and the other on the right).

A variation of this device is obtained by replacing contact 1 (together with the CISS molecules underneath it) with a ferromagnet, as shown in the inset of Fig. 8(a). This variation allows one to control the sign of R_{nl} by controlling the magnetization direction of the ferromagnet, which should be aligned parallel or antiparallel to the helical (chiral) axis of the CISS molecules (out of plane, as indicated by the arrows). The nonlocal resistance is therefore

$$R_{nl}(\uparrow) = -R_{nl}(\downarrow) = P_{FM}k_{det}R_{\lambda}e^{-\frac{d}{\lambda_s}}, \quad (18)$$

where the arrows indicate the magnetization directions, P_{FM} is the polarization of the ferromagnet, and R_{λ} is the spin resistance of graphene (see Appendix B for more details). In this device, the reversal of the magnetization direction of the ferromagnet leads to a sign change of the nonlocal resistance. Under experimental conditions [42,43], this nonlocal resistance change $\Delta R_{nl} = R_{nl}(\uparrow) - R_{nl}(\downarrow)$ can reach tens of Ohms (Ω) and is easily detectable.

The second type of device is depicted in Fig. 8(b). It is a variation of the geometry in Fig. 7, where contact 2 is replaced by a ferromagnet. In this device, instead of traveling through the CISS molecules, the electrons travel through the graphene channel underneath the molecules. It is assumed that due to the proximity of the CISS molecules, the electrons in graphene also experience a (weaker) CISS effect. Whether this assumption is valid remains to be proven. The nonlocal signals produced by this device are derived in Appendix B.

IV. CONCLUSION

In summary, we demonstrated that a spin-flip electron reflection process is inherent to the chiral induced spin selectivity (CISS) effect in linear-regime electron transport. Furthermore, we developed a set of spin-dependent electron transmission and reflection matrices and a generalized barrier-CISS center-barrier (BCB) model to quantitatively describe the CISS effect in mesoscopic devices. Based on this formalism, we demonstrated that more than two terminals are needed in order to probe the CISS effect in linear-regime transport experiments. Moreover, we also showed several ways of injecting and detecting spins using CISS molecules and demonstrated that CISS molecules can give rise to spin-charge conversion. In addition, we proposed two types of graphene-based nonlocal devices which can be used to directly measure the CISS effect in the linear regime.

We stress again that the above discussions and proposed devices are all based on linear-regime electron transport. Therefore, our conclusions cannot exclude the two-terminal detection of the CISS effect in the nonlinear regime. However, the spin signals in nonlinear-regime measurements should approach zero as the two-terminal bias approaches zero (entering the linear regime), and the mechanism that may con-

tribute to such signals has to be different from spin-dependent electron transmission and reflection. A recent work shows that the CISS effect in electron photoemission experiments (three terminal) can be explained by losses due to spin-dependent electron absorption in chiral molecules [44], but whether a similar process can lead to the detection of the CISS effect in nonlinear two-terminal measurements remains to be investigated. In general, our model captures the fundamental role of the CISS effect in linear-regime mesoscopic devices without assuming any microscopic electron transport mechanism inside CISS molecules. Recently, a new type of spin-orbit coupling was predicted for one-dimensional screw dislocations in semiconductor crystals, which has a one-dimensional helical effective electric field. This type of spin-orbit coupling can lead to an enhanced spin lifetime for electrons traveling along the helical axis [45]. Future theoretical work should study whether similar effects exist in chiral or helical molecules.

In general, our model helps to analyze and understand device-based CISS experiments without having to understand the CISS effect on a molecular level. It provides a guideline for future reviewing and designing of CISS-based mesoscopic spintronic devices.

ACKNOWLEDGMENTS

The authors acknowledge the financial support from the Zernike Institute for Advanced Materials (ZIAM), and the Spinoza prize awarded to Professor B. J. van Wees by the Nederlandse Organisatie voor Wetenschappelijk Onderzoek (NWO). X.Y. acknowledges helpful discussions with G. E. W. Bauer, V. Mujica, H. Zacharias, and R. Naaman.

APPENDIX A: GENERAL VALIDITY OF THE SPIN-FLIP REFLECTION PROCESS

In the main text, we stated that a spin-flip electron reflection process has to exist in order for spin-dependent transmission through CISS molecules to be allowed by the reciprocity theorem. Mathematically, this statement means that at least one off-diagonal term in the reflection matrices of CISS molecules has to be nonzero. Now, we prove the general validity of our statement by limiting all off-diagonal terms of the reflection matrices to zero, and derive violations against the description of the CISS effect. Under this limit, the general form of the transmission and reflection matrices of a CISS molecule is

$$\mathbb{T}_{\text{CISS}} = \begin{pmatrix} a & c \\ b & d \end{pmatrix}, \quad \mathbb{R}_{\text{CISS}} = \begin{pmatrix} A & 0 \\ 0 & D \end{pmatrix}, \quad (\text{A1})$$

where $0 \leq a, b, c, d, A, D \leq 1$. For electrons traveling towards the CISS molecule, each spin component can either be transmitted (with or without spin flip) or reflected, the sum of these probabilities is therefore unity:

$$a + b + A = 1, \quad c + d + D = 1. \quad (\text{A2})$$

Therefore, we have

$$\mathbb{R}_{\text{CISS}} = \begin{pmatrix} 1 - a - b & 0 \\ 0 & 1 - c - d \end{pmatrix}. \quad (\text{A3})$$

In addition, we adopt transmission and reflection matrices of a ferromagnet from Fig. 2.

Next, we consider that the CISS effect exists in the linear regime. This means that (according to the description of the CISS effect) with an input of spin-nonpolarized electrons, the CISS molecule gives a spin-polarized transmission output (a nonzero spin current I_s). Here, we do not make assumptions about the chirality of the molecule or the electron flow direction, so that our conclusions hold for the most general situations. Therefore, we do not assume the sign of I_s , and write

$$I_s = (1, -1)\mathbb{T}_{\text{CISS}} \begin{pmatrix} 1/2 \\ 1/2 \end{pmatrix} = \frac{(a+c) - (b+d)}{2} \neq 0, \quad (\text{A4})$$

where the column vector indicates the spin-nonpolarized input current, and the row vector is an operator that calculates the difference between the two spin components in the output current.

In order to illustrate the discrepancy between the assumption of not having any spin-flip reflection and the conceptual description of the CISS effect [Eq. (A4)], we apply the reciprocity theorem to the circuit segment shown in Fig. 1. For this circuit segment, we calculate the total transmission matrix accounting for the contribution from both the CISS molecule and the ferromagnet, and obtain

$$\mathbb{T}_{21} = \mathbb{T}_{\text{FM}} \cdot (\mathbb{I} - \mathbb{R}_{\text{CISS}} \cdot \mathbb{R}_{\text{FM}})^{-1} \cdot \mathbb{T}_{\text{CISS}}. \quad (\text{A5})$$

The transmission probability accounting for both spin species is therefore

$$T_{21} = (1, 1)\mathbb{T}_{21} \begin{pmatrix} 1/2 \\ 1/2 \end{pmatrix}, \quad (\text{A6})$$

where the row vector is an operator that calculates the sum of both spin species. By substituting the matrices, we can write T_{21} as a function of P_{FM} :

$$T_{21}(P_{\text{FM}}) = \frac{a(1 + P_{\text{FM}})}{1 + a + b + P_{\text{FM}}(1 - a - b)} + \frac{d(1 - P_{\text{FM}})}{1 + c + d - P_{\text{FM}}(1 - c - d)}. \quad (\text{A7})$$

Here, the magnetization reversal of the ferromagnet is equivalent to a sign change of P_{FM} . Therefore, the broader reciprocity theorem requires [36,37]

$$T_{12}(P_{\text{FM}}) \equiv T_{12}(-P_{\text{FM}}) \quad (\text{A8})$$

for all $0 < |P_{\text{FM}}| \leq 1$. This requirement gives

$$a = d \text{ and } b = c,$$

and, therefore,

$$(a + c) - (b + d) = 0,$$

which violates Eq. (A4).

Therefore, we proved that the spin-flip electron reflection process has to exist in order for the CISS effect to exist in the linear transport regime, and this is a direct requirement from the reciprocity theorem.

APPENDIX B: FURTHER DISCUSSIONS ABOUT THE BCB MODEL

1. Derivation of the BCB transmission and reflection matrices

In the BCB model, we consider a CISS molecule as two normal barriers sandwiching an ideal CISS center. The three parts together determine the transmission and reflection matrices of the molecule. We derive these matrices in two steps. First, we calculate the combined contribution of the leftmost barrier and the ideal CISS center as part 1 (superscript $P1$). Then, we add the second barrier to part 1 and calculate the total effect.

We adopt the transmission and reflection matrices for a normal barrier and a CISS center from Fig. 2. Here, we only discuss P -type CISS molecules, as the AP type can be derived using the relations given in Fig. 2. For part 1 we have

$$\mathbb{T}_R^{P1} = (\mathbb{T}_{0,R}^P + \mathbb{T}_{0,R}^P \cdot \mathbb{R}_B \cdot \mathbb{R}_{0,R}^P) \cdot \mathbb{T}_B = \begin{pmatrix} t & t(1-t) \\ 0 & 0 \end{pmatrix}, \quad (\text{B1a})$$

$$\mathbb{R}_R^{P1} = \mathbb{R}_B + \mathbb{T}_B \cdot \mathbb{R}_{0,R}^P \cdot \mathbb{T}_B = \begin{pmatrix} 1-t & t^2 \\ 0 & 1-t \end{pmatrix}, \quad (\text{B1b})$$

$$\mathbb{T}_L^{P1} = (\mathbb{T}_B + \mathbb{T}_B \cdot \mathbb{R}_{0,R}^P \cdot \mathbb{R}_B) \cdot \mathbb{T}_{0,L}^P = \begin{pmatrix} 0 & t(1-t) \\ 0 & t \end{pmatrix}, \quad (\text{B1c})$$

$$\mathbb{R}_L^{P1} = \mathbb{R}_{0,L}^P + \mathbb{T}_{0,R}^P \cdot \mathbb{R}_B \cdot \mathbb{R}_{0,R}^P \cdot \mathbb{R}_B \cdot \mathbb{T}_{0,L}^P = \begin{pmatrix} 0 & (1-t)^2 \\ 1 & 0 \end{pmatrix}. \quad (\text{B1d})$$

Note that here we have a finite number of reflections between the first barrier and the CISS center because the CISS center is ideal. Now, we consider part 1 as one unit and combine it with the second normal barrier

$$\begin{aligned} \mathbb{T}_R^P &= \mathbb{T}_B \cdot (\mathbb{I} - \mathbb{R}_L^{P1} \cdot \mathbb{R}_B)^{-1} \cdot \mathbb{T}_R^{P1} \\ &= \begin{pmatrix} \sigma/(1-t) & \sigma \\ \sigma & \sigma(1-t) \end{pmatrix}, \end{aligned} \quad (\text{B2a})$$

$$\begin{aligned} \mathbb{R}_R^P &= \mathbb{R}_R^{P1} + \mathbb{T}_L^{P1} \cdot (\mathbb{I} - \mathbb{R}_B \cdot \mathbb{R}_L^{P1})^{-1} \cdot \mathbb{R}_B \cdot \mathbb{T}_R^{P1} \\ &= \begin{pmatrix} \sigma(1-t)^2 - t + 1 & \sigma/(1-t) \\ \sigma(1-t) & \sigma(1-t)^2 - t + 1 \end{pmatrix}, \end{aligned} \quad (\text{B2b})$$

$$\begin{aligned} \mathbb{T}_L^P &= \mathbb{T}_L^{P1} \cdot (\mathbb{I} - \mathbb{R}_B \cdot \mathbb{R}_L^{P1})^{-1} \cdot \mathbb{T}_B \\ &= \begin{pmatrix} \sigma(1-t) & \sigma \\ \sigma & \sigma/(1-t) \end{pmatrix}, \end{aligned} \quad (\text{B2c})$$

$$\begin{aligned} \mathbb{R}_L^P &= \mathbb{R}_B + \mathbb{T}_B \cdot (\mathbb{I} - \mathbb{R}_L^{P1} \cdot \mathbb{R}_B)^{-1} \cdot \mathbb{R}_L^{P1} \cdot \mathbb{T}_B \\ &= \begin{pmatrix} \sigma(1-t)^2 - t + 1 & \sigma(1-t) \\ \sigma/(1-t) & \sigma(1-t)^2 - t + 1 \end{pmatrix}, \end{aligned} \quad (\text{B2d})$$

$$\text{where } \sigma = \frac{t^2(1-t)}{-t^4 + 4t^3 - 6t^2 + 4t}.$$

These results show that in the BCB model, one parameter t ($0 < t \leq 1$) determines the entire set of transmission and

reflection probability matrices. Therefore, it is possible to plot total electron transmission and reflection probabilities as a function of t for various geometries, as shown below. With different t values, the BCB model is able to represent a large spectrum of CISS molecules with different “strengths” of the CISS effect. While it is sufficient to illustrate the fundamental role of a CISS molecule in a solid-state device, it is still a simplified picture. We will introduce a more generalized model later in Appendix C.

2. Discussion on the FM-BCB geometry

In the main text, we discussed that the two-terminal transmission remains constant under magnetization reversal in the FM-BCB geometry, here we illustrate the same result under current reversal. (Note that this is also a restriction from the linear regime.)

The transmission and reflection matrices from contact 2 to contact 1 are

$$\mathbb{T}_{12}^{\text{FM-BCB}}(\Rightarrow) = \mathbb{T}_{\text{FM}}(\Rightarrow) \cdot (\mathbb{I} - \mathbb{R}_R^P \cdot \mathbb{R}_{\text{FM}}(\Rightarrow))^{-1} \cdot \mathbb{T}_L^P, \quad (\text{B3a})$$

$$\begin{aligned} \mathbb{R}_{22}^{\text{FM-BCB}}(\Rightarrow) &= \mathbb{R}_L^P + \mathbb{T}_R^P \cdot (\mathbb{I} - \mathbb{R}_{\text{FM}}(\Rightarrow) \cdot \mathbb{R}_R^P)^{-1} \\ &\quad \cdot \mathbb{R}_{\text{FM}}(\Rightarrow) \cdot \mathbb{T}_L^P, \end{aligned} \quad (\text{B3b})$$

and the corresponding transmission and reflection probabilities accounting for both spins are

$$T_{12}^{\text{FM-BCB}}(\Rightarrow) = (1, 1) \mathbb{T}_{12}^{\text{FM-BCB}}(\Rightarrow) \begin{pmatrix} 1/2 \\ 1/2 \end{pmatrix}, \quad (\text{B4a})$$

$$R_{22}^{\text{FM-BCB}}(\Rightarrow) = (1, 1) \mathbb{R}_{22}^{\text{FM-BCB}}(\Rightarrow) \begin{pmatrix} 1/2 \\ 1/2 \end{pmatrix}. \quad (\text{B4b})$$

With these expressions, we can calculate the transmission and reflection probabilities as a function of t (BCB transmission probability) for four situations: two current directions and two magnetization directions, and the results are plotted in Fig. 9. Note that for all four situations, the transmission curves (or the reflection curves) completely overlap with each other, this means that neither magnetization reversal nor current reversal can lead to a signal change in the two-terminal conductance. Furthermore, we are able to quantitatively analyze the contribution of each spin component in each of the four situations, and this will be shown in the Supplemental Material [46].

3. Discussion on the spin-valve geometry

Similar to the FM-BCB geometry, in order to calculate the two-terminal transmission and reflection probability of the spin-valve geometry, we first calculate the transmission and reflection matrices for this geometry. For this, we treat the spin-valve geometry as an FM-BCB module and a ferromagnet connected in series, and derive

$$\begin{aligned} \mathbb{T}_{21}^{\text{SV}}(\Rightarrow, \Rightarrow) &= \mathbb{T}_{\text{FM}}(\Rightarrow) \cdot (\mathbb{I} - \mathbb{R}_{22}^{\text{FM-BCB}}(\Rightarrow) \cdot \mathbb{R}_{\text{FM}}(\Rightarrow))^{-1} \\ &\quad \cdot \mathbb{T}_{21}^{\text{FM-BCB}}(\Rightarrow), \end{aligned} \quad (\text{B5a})$$

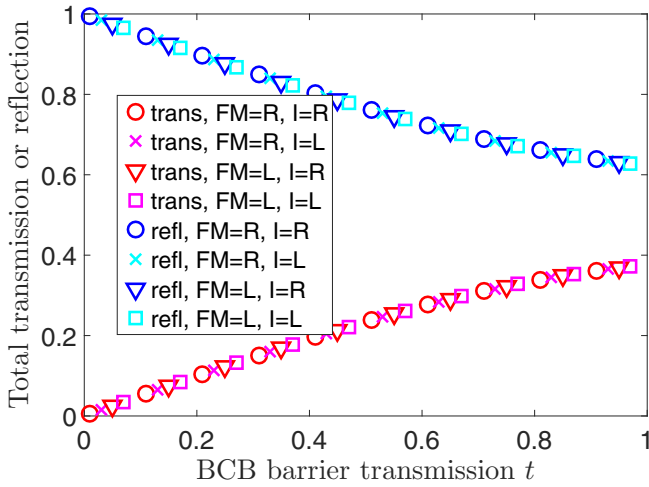


FIG. 9. Normalized total transmission and reflection of an FM-BCB segment as a function of t (BCB barrier transmission). Red and magenta labels (lower group) are for total transmissions accounting for both spin species for different magnetization orientations (FM = R or L , for magnetization *right* or *left*) and different electron flow directions ($I = R$ or L , for electron flow from *left to right* or from *right to left*). Blue and cyan labels (upper group) are for total reflections. The polarization of the ferromagnet is chosen as $P_{\text{FM}} = 0.1$, comparable to experimental conditions with Co contacts.

$$\begin{aligned} \mathbb{R}_{11}^{SV}(\Rightarrow, \Rightarrow) &= \mathbb{R}_{11}^{\text{FM-BCB}}(\Rightarrow) + \mathbb{T}_{21}^{\text{FM-BCB}}(\Rightarrow) \cdot (\mathbb{I} - \mathbb{R}_{\text{FM}}(\Rightarrow)) \\ &\quad \cdot \mathbb{R}_{22}^{\text{FM-BCB}}(\Rightarrow)^{-1} \\ &\quad \cdot \mathbb{R}_{\text{FM}}(\Rightarrow) \cdot \mathbb{T}_{12}^{\text{FM-BCB}}(\Rightarrow), \end{aligned} \quad (\text{B5b})$$

$$\begin{aligned} \mathbb{T}_{12}^{SV}(\Rightarrow, \Rightarrow) &= \mathbb{T}_{12}^{\text{FM-BCB}}(\Rightarrow) \cdot (\mathbb{I} - \mathbb{R}_{\text{FM}}(\Rightarrow) \cdot \mathbb{R}_{22}^{\text{FM-BCB}}(\Rightarrow))^{-1} \\ &\quad \cdot \mathbb{T}_{\text{FM}}(\Rightarrow), \end{aligned} \quad (\text{B5c})$$

$$\begin{aligned} \mathbb{R}_{22}^{SV}(\Rightarrow, \Rightarrow) &= \mathbb{R}_{\text{FM}}(\Rightarrow) + \mathbb{T}_{\text{FM}}(\Rightarrow) \\ &\quad \cdot (\mathbb{I} - \mathbb{R}_{22}^{\text{FM-BCB}}(\Rightarrow) \cdot \mathbb{R}_{\text{FM}}(\Rightarrow))^{-1} \\ &\quad \cdot \mathbb{R}_{22}^{\text{FM-BCB}}(\Rightarrow) \cdot \mathbb{T}_{\text{FM}}(\Rightarrow), \end{aligned} \quad (\text{B5d})$$

where the two arrows in the brackets on the left-hand side of the equations indicate the magnetization direction of the two ferromagnets, respectively. For the case where the magnetization of one of the ferromagnets is reversed, we can substitute the corresponding magnetization direction with an opposite arrow.

For the two-terminal transmission and reflection probabilities accounting for both spins, we have

$$T_{ij}^{SV} = (1, 1) \cdot \mathbb{T}_{ij}^{SV} \cdot \begin{pmatrix} 1/2 \\ 1/2 \end{pmatrix}, \quad (\text{B6a})$$

$$R_{ij}^{SV} = (1, 1) \cdot \mathbb{R}_{ij}^{SV} \cdot \begin{pmatrix} 1/2 \\ 1/2 \end{pmatrix}, \quad (\text{B6b})$$

and we can calculate these probabilities as a function of t (BCB transmission probability) for eight situations: the two

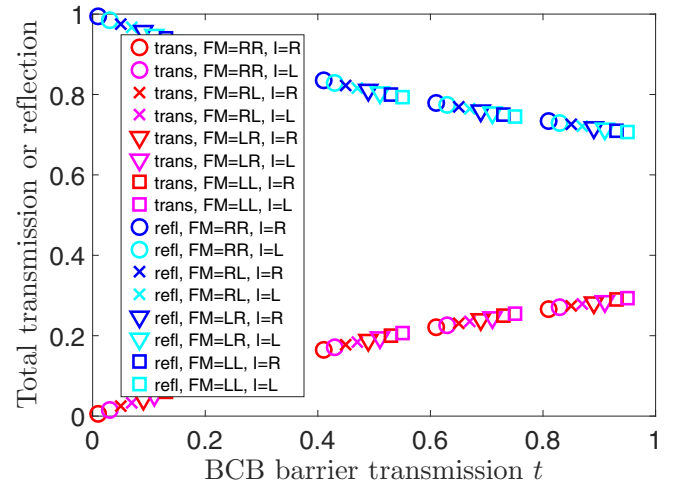


FIG. 10. Normalized total transmission and reflection of a spin-valve segment as a function of t (BCB barrier transmission). Red and magenta labels (lower group) are for total transmissions accounting for both spin species for different ferromagnet configurations (similar notation as before, but for two ferromagnets, FM = RR , RL , LR , or LL) and different current flow directions ($I = R$ or L). Blue and cyan labels (upper group) are for total reflections. The polarization of the ferromagnet is chosen as $P_{\text{FM}} = 0.1$, comparable to experimental conditions with Co contacts.

ferromagnets each with two magnetization directions, and two opposite current directions, as shown in Fig. 10. Note that for all eight situations, the transmission curves (or the reflection curves) completely overlap with each other; this means that neither magnetization reversal (for either ferromagnet) nor current reversal can lead to a signal change in the two-terminal conductance. Furthermore, we can quantitatively analyze the contribution of each spin component in this geometry, as shown in the Supplemental Material [46].

4. Discussion on injection and detection coefficients

In the main text, we derived the injection and detection coefficients k_{inj} and k_{det} for the four-terminal geometry shown

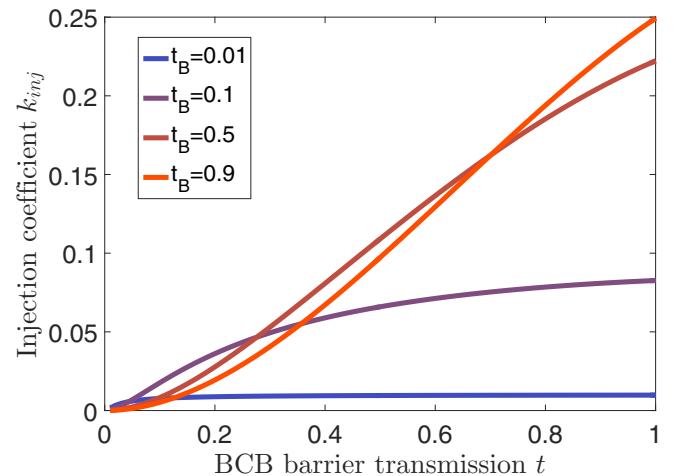


FIG. 11. Injection coefficient k_{inj} as a function of t (BCB barrier transmission) for various t_B (contact barrier transmission), for the geometry described in Fig. 6(a) in the main text.

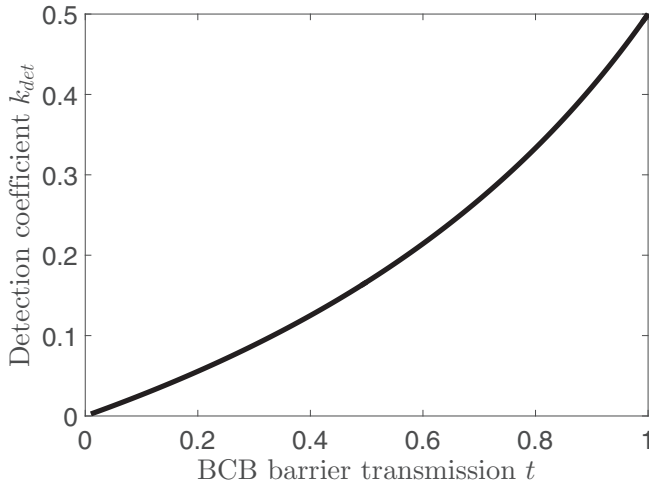


FIG. 12. Detection coefficient k_{det} as a function of t (BCB barrier transmission) for the geometry described in Fig. 6(a) in the main text.

in Fig. 6(a), and we showed that the product of these two geometries represents the ratio between four-terminal and two-terminal resistances. The injection coefficient depends both on the BCB barrier transmission t and the transmission probability t_B of the barrier at contact 2, whereas the detection coefficient only depends on the BCB barrier transmission t . This difference is due to our assumption of weakly coupled detection contacts. Here, we plot the injection coefficient k_{inj} (see Fig. 11), the detection coefficient k_{det} (see Fig. 12), and the $4T/2T$ resistance ratio R_{4T}/R_{2T} (see Fig. 13) as a function of t (transmission probability of the barrier in the BCB molecule). Especially, for k_{inj} and R_{4T}/R_{2T} , we set t_B (transmission probability of the barrier in contact 2) to a few different values and illustrate its influence.

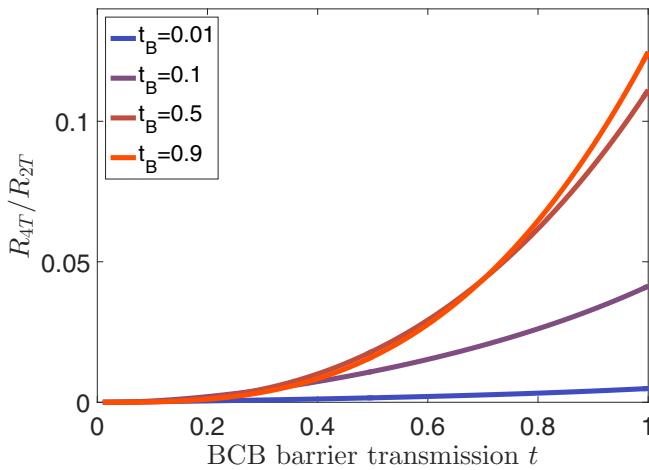


FIG. 13. The ratio between four-terminal and two-terminal resistances as a function of t (BCB barrier transmission) for various t_B (contact barrier transmission), for the geometry described in Fig. 6(a) in the main text.

5. Discussion on spin-charge conversion

In the main text, we illustrated the spin-charge conversion property of CISS molecules. The chemical potential vectors in the two nodes in Fig. 7 are related to each other following Eq. (16). We also introduced the scalars of charge chemical potential μ_n (the average of two spin chemical potentials) and spin accumulation μ_s (the difference between two spin chemical potentials). Here, we show how these scalar chemical potentials relate to each other.

A vector chemical potential of a node can be rewritten as a sum of two column vectors

$$\boldsymbol{\mu} = \begin{pmatrix} \mu_{\rightarrow} \\ \mu_{\leftarrow} \end{pmatrix} = \begin{pmatrix} \mu_n + \frac{1}{2}\mu_s \\ \mu_n - \frac{1}{2}\mu_s \end{pmatrix} = \mu_n \begin{pmatrix} 1 \\ 1 \end{pmatrix} + \frac{1}{2}\mu_s \begin{pmatrix} 1 \\ -1 \end{pmatrix}. \quad (\text{B7})$$

By rewriting both $\boldsymbol{\mu}_A$ and $\boldsymbol{\mu}_B$ in this fashion, and substituting them into Eq. (16), we obtain

$$\Delta\mu_n \begin{pmatrix} 1 \\ 1 \end{pmatrix} + \frac{1}{2}\Delta\mu_s \begin{pmatrix} 1 \\ -1 \end{pmatrix} = (\mathbb{I} - (\mathbb{I} - \mathbb{R}_L^P)^{-1} \mathbb{T}_R^P) \boldsymbol{\mu}_A, \quad (\text{B8})$$

where $\Delta\mu_n = \mu_{nA} - \mu_{nB}$ is the charge chemical potential difference between the two nodes, and $\Delta\mu_s = \mu_{sA} - \mu_{sB}$ is the spin accumulation difference between the two nodes.

For the BCB model,

$$\mathbb{I} - (\mathbb{I} - \mathbb{R}_L^P)^{-1} \mathbb{T}_R^P = \begin{pmatrix} 1 + \frac{1}{t-2} & -1 - \frac{1}{t-2} \\ \frac{1}{t-2} & -\frac{1}{t-2} \end{pmatrix}, \quad (\text{B9})$$

where t is the BCB transmission probability. Substituting this matrix into Eq. (B8) gives

$$\Delta\mu_n \begin{pmatrix} 1 \\ 1 \end{pmatrix} + \frac{1}{2}\Delta\mu_s \begin{pmatrix} 1 \\ -1 \end{pmatrix} = \mu_{sA} \begin{pmatrix} 1 + \frac{1}{t-2} \\ \frac{1}{t-2} \end{pmatrix}. \quad (\text{B10})$$

Note that here the charge chemical potentials in node A (μ_{nA}) drops out of the equation. We emphasize that this is a unique result for the BCB model.

Solving the above vector equation gives

$$\Delta\mu_s = \mu_{sA}, \quad (\text{B11a})$$

$$\Delta\mu_n = -k_{\text{conv}} \Delta\mu_s, \quad (\text{B11b})$$

where $k_{\text{conv}} = t/(4-2t)$ ($0 < k_{\text{conv}} \leq 0.5$) is the spin-charge conversion coefficient.

Equation (B11a) shows that $\mu_{sB} = \mu_{sA} - \Delta\mu_s = 0$, meaning that a spin accumulation in node A cannot generate a spin accumulation in node B . This result is special for the BCB model and does not hold for a more generalized CISS model (as will be introduced later in Appendix C). Equation (B11b) shows that the charge voltage across a BCB molecule linearly depends on the spin accumulation difference across the molecule, and vice versa (spin-charge conversion). The conversion coefficient k_{conv} depends on t (BCB barrier transmission). Notably, for BCB molecules this coefficient has the same value as the detection coefficient ($k_{\text{conv}} = k_{\text{det}}$). This is because the result $\mu_{sB} = 0$ makes node B equivalent to a contact: it is not able to distinguish between two spin components. For a more generalized model (as will be introduced later in Appendix C), the two coefficients take different values. These

conclusions were mentioned in the main text; here we showed the proof.

6. Discussion on nonlocal signals

We first discuss the nonlocal resistance measured with device geometries shown in Fig. 8(a). In this picture the axes of the CISS molecules are vertical rather than horizontal, therefore, the spin orientations are described as spin up or spin down. As a result, the spin accumulation is defined as $\mu_s = (\mu_\uparrow - \mu_\downarrow)$.

First, we discuss the case where the spin injection is done through a BCB molecule. The injected spin accumulation underneath contact 1 is

$$\mu_{s,inj} = -k_{inj}\mu_1 = -e k_{inj} I_{inj} R_{inj}, \quad (\text{B12})$$

where the minus sign is due to the fact that the electrons are traveling downwards through CISS molecules into graphene, as a result, the injected spin accumulation is negative (mostly spin down). The resistance

$$R_{inj} = R_{12} = \frac{\mu_1 - \mu_2}{e I_{inj}} \quad (\text{B13})$$

is the resistance measured between the two injection contacts 1 and 2.

Inside graphene, the spin accumulation diffuses to all directions, and therefore the spin accumulation at the detection contact is

$$\mu_{s,det} = \mu_{s,inj} e^{-\frac{d}{\lambda_s}}, \quad (\text{B14})$$

where λ_s is the spin diffusion length in graphene, and d is the distance between the inner injection and detection contacts (1 and 4) (we have assumed that this distance is much larger than the separation of the two injection contacts or the separation of the two detection contacts).

Further, the voltage detected by the detection contacts is [following Eq. (13)]

$$V_{det} = \frac{1}{e} k_{det} \mu_{s,det}. \quad (\text{B15})$$

With this, we have

$$R_{nl} = \frac{V_{det}}{I_{inj}} = -k_{inj} k_{det} R_{inj} e^{-\frac{d}{\lambda_s}}, \quad (\text{B16})$$

as in Eq. (17).

For the case where the spin injection is obtained through a ferromagnet, the spin injection becomes

$$\mu_{s,inj} = \pm e P_{FM} I_{inj} R_\lambda, \quad (\text{B17})$$

where P_{FM} is the polarization of the ferromagnet (with magnetization direction out of plane), and R_λ is the spin resistance of graphene. This spin resistance is determined by the spin relaxation length in graphene and the shape of the graphene channel, and is defined as $R_\lambda = R_{sq} \lambda_s / W$, where R_{sq} is the square resistance of graphene and W is the width of the graphene channel (assuming the channel width remains the same across the spin diffusion length). The sign of the injected spin accumulation is determined by the magnetization direction of the ferromagnet, with magnetization up for positive spin accumulation and magnetization down for negative spin accumulation.

The diffusion and detection mechanisms are the same as in the previous case. Therefore, the nonlocal resistance for this situation is

$$R_{nl} = \pm k_{det} P_{FM} R_\lambda e^{-\frac{d}{\lambda_s}}, \quad (\text{B18})$$

as in Eq. (18). With the help of the ferromagnet, it is possible to switch the sign of the nonlocal resistance.

Next, for the device shown in Fig. 8(b), the CISS molecules are aligned in plane of the device, therefore, we assume the ferromagnet also has in-plane magnetization, and we describe spin accumulation again as $\mu_s = \mu_\rightarrow - \mu_\leftarrow$. We simplify the discussion by assuming the spin injection is mainly contributed by the ferromagnet, and the spin detection is achieved through the spin-charge conversion mechanism of the CISS molecules. The spin accumulation underneath the detection contacts can be generated by two mechanisms: the spin diffusion in graphene (as in the previous case), and the spin-charge conversion between the injection node and the detection node. However, in the BCB model, the spin-charge conversion does not contribute to a spin accumulation underneath the detector contacts. Therefore, we only consider the spin diffusion mechanism. Similar to the previous case, we can derive the nonlocal signal

$$R_{nl} = \pm k_{conv} P_{FM} R_\lambda e^{-\frac{d}{\lambda_s}}, \quad (\text{B19})$$

where k_{conv} is the spin-charge conversion coefficient described before, but here it concerns the proximity-induced CISS effect in the graphene channel, rather than the CISS molecules themselves. Important to realize, due to the proximity effect, the diffusion length λ_s and the spin resistance R_λ of graphene may differ from the previous case.

APPENDIX C: GENERALIZED CISS MODEL

The BCB model is a simplified model where the spin-dependent characteristics of a CISS molecule are exclusively originated from an ideal CISS center. However, the assumption of having an ideal spin-flip core in a molecule may not be accurate. Therefore, we assume a general form of transmission and reflection matrices

$$\mathbb{T}_R^P = \begin{pmatrix} a, c \\ b, d \end{pmatrix}, \quad \mathbb{R}_R^P = \begin{pmatrix} A, C \\ B, D \end{pmatrix}, \quad (\text{C1})$$

where

$$0 \leq a, b, c, d, A, B, C, D \leq 1, \quad (\text{C2a})$$

$$a + b + A + B = c + d + C + D = 1, \quad (\text{C2b})$$

$$a + c > b + d. \quad (\text{C2c})$$

Here, the first restriction (C2a) comes from the fact that all matrix elements are probabilities. The second restriction (C2b) addresses that for each spin component, the sum of its probabilities of being transmitted and being reflected equals 1. The third restriction (C2c) is the conceptual description of the CISS effect, which shows that a spin polarization arises after transmission through a CISS molecule. This restriction is similar to Eq. (A4), but here we determine a sign for

the polarization because we have assumed the chirality (P type) of the molecule and the electron flow direction (R for rightwards).

We still assume that the molecule has C_2 symmetry, so that the transmission and reflection matrices for reversed current can be written as

$$\mathbb{T}_L^P = \begin{pmatrix} 0 & 1 \\ 1 & 0 \end{pmatrix} \cdot \mathbb{T}_R^P \cdot \begin{pmatrix} 0 & 1 \\ 1 & 0 \end{pmatrix}, \quad (\text{C3a})$$

$$\mathbb{R}_L^P = \begin{pmatrix} 0 & 1 \\ 1 & 0 \end{pmatrix} \cdot \mathbb{R}_R^P \cdot \begin{pmatrix} 0 & 1 \\ 1 & 0 \end{pmatrix}. \quad (\text{C3b})$$

The matrices for AP -type molecules can be derived according to Fig. 2. Before we proceed with the mathematical proof, we discuss the validity of these symmetry assumptions.

Since we only consider the electron transport in CISS molecules, the C_2 symmetry that we require only refers to the symmetry in electron transport. Furthermore, this symmetry is also a requirement of the linear regime. A highly asymmetric molecule can still be treated with our model, but only under the assumption that it is composed of a symmetric (C_2) part which contributes to CISS, and asymmetrically distributed normal barriers. In terms of the symmetry relations between the two chiralities, it is by definition that the two chiral enantiomers are exact mirror images of each other, and thereby select opposite spins with equal probability (when placed in the same circuit environment).

We apply the reciprocity theorem to a geometry similar to Fig. 4 in the main text, but now the BCB molecule is replaced by a generalized CISS molecule. The general reciprocity theorem requires that the two-terminal resistance remains unchanged under magnetization reversal regardless of the polarization of the ferromagnet. Therefore, we assume the ferromagnet is 100% polarized for convenience. Following the same steps as in the FM-BCB geometry, the two-terminal transmission probabilities considering two magnetization directions and two current directions become

$$T_{21}(\Rightarrow) = a + b + (c + d) \frac{B}{1 - D}, \quad (\text{C4a})$$

$$T_{21}(\Leftarrow) = c + d + (a + b) \frac{C}{1 - A}, \quad (\text{C4b})$$

$$T_{12}(\Rightarrow) = b + d + (a + c) \frac{C}{1 - D}, \quad (\text{C4c})$$

$$T_{12}(\Leftarrow) = a + c + (b + d) \frac{B}{1 - A}, \quad (\text{C4d})$$

where the arrows indicate the magnetization direction of the ferromagnet, and the subscripts indicate the electron flow direction. The reciprocity theorem requires these four expressions to have the same value

$$T_{12}(\Rightarrow) = T_{12}(\Leftarrow) = T_{21}(\Rightarrow) = T_{21}(\Leftarrow) = T, \quad (\text{C5})$$

which can be written as a vector equation

$$\begin{pmatrix} 1 & 1 & \frac{B}{1-D} & \frac{B}{1-D} \\ \frac{C}{1-A} & \frac{C}{1-A} & 1 & 1 \\ \frac{C}{1-D} & 1 & \frac{C}{1-D} & 1 \\ 1 & \frac{B}{1-A} & 1 & \frac{B}{1-A} \end{pmatrix} \begin{pmatrix} a \\ b \\ c \\ d \end{pmatrix} = T \begin{pmatrix} 1 \\ 1 \\ 1 \\ 1 \end{pmatrix}. \quad (\text{C6})$$

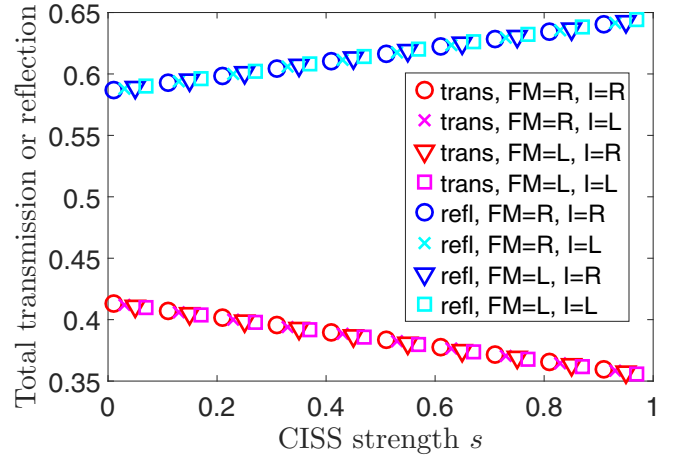


FIG. 14. Normalized total transmission and reflection of an FM-CISS segment as a function of s (generalized CISS strength). Red and magenta labels (lower group) are for total transmissions accounting for both spin species for different magnetization orientations (FM = R or L) and different electron flow directions ($I = R$ or L). Blue and cyan labels (upper group) are for total reflections. The polarization of the ferromagnet is chosen as $P_{\text{FM}} = 0.7$ to be consistent with Fig. 15.

In order for this equation to be self-consistent, relation

$$A = D$$

is required. Consequently, we can derive

$$b = c, \quad (\text{C7a})$$

$$a - d = C - B. \quad (\text{C7b})$$

Therefore, the generalized form of the transmission and reflection matrices of a CISS molecule is

$$\mathbb{T}_R^P = \begin{pmatrix} a & b \\ b & a(1-s) \end{pmatrix}, \quad \mathbb{R}_R^P = \begin{pmatrix} A & B + as \\ B & A \end{pmatrix}, \quad (\text{C8})$$

with $a + b + A + B = 1$, and s ($0 \leq s \leq 1$) being a quantitative description of the *strength* of the CISS effect in a molecule.

Next, we discuss the results given by this generalized model for the geometries discussed in the main text, and compare it with the BCB model. We arbitrarily choose the following transmission and reflection matrices for the generalized model:

$$\mathbb{T}_R^P = \begin{pmatrix} 0.6 & 0.15 \\ 0.15 & 0.6(1-s) \end{pmatrix}, \quad \mathbb{R}_R^P = \begin{pmatrix} 0.2 & 0.05 + 0.6s \\ 0.05 & 0.2 \end{pmatrix}, \quad (\text{C9})$$

and use parameter s as the variable to tune the CISS strength.

For the FM-BCB geometry (which now becomes FM-CISS geometry), we plot the two-terminal transmission and reflection probabilities as a function of s for four situations: two magnetization directions and two current directions. The results show that all four situations give identical results for all CISS strength s , as shown in Fig. 14. This is consistent with the BCB model, just as required by the reciprocity theorem.

For the spin-valve geometry, we plot the two-terminal transmission and reflection probabilities as a function of s

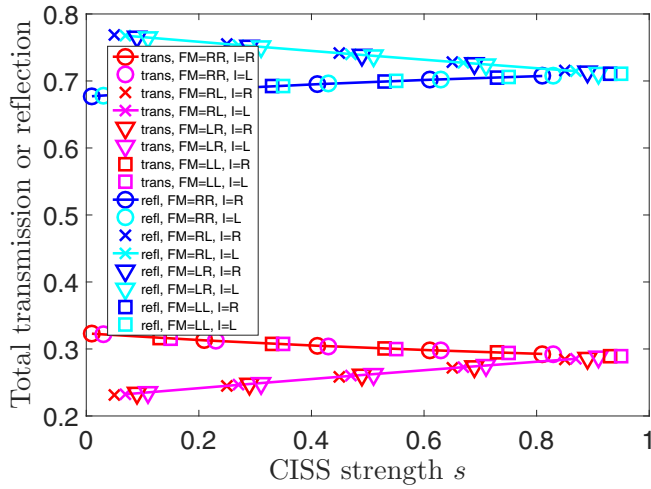


FIG. 15. Normalized total transmission and reflection of a spin-valve segment as a function of s (generalized CISS strength). Red and magenta labels (lower group) are for total transmissions accounting for both spin species for different ferromagnet configurations (two ferromagnets, $FM = RR, RL, LR, \text{ or } LL$) and different current flow directions ($I = R$ or L). Blue and cyan labels (upper group) are for total reflections. The polarization of the ferromagnet is chosen as $P_{FM} = 0.7$ in order to amplify the deviation between parallel and antiparallel ferromagnet configurations. This deviation is larger when the ferromagnet polarization is higher.

for eight situations: two ferromagnets each with two magnetization directions, and two current directions. The results are shown in Fig. 15. Unlike the BCB model, here we find different transmission and reflection probabilities for cases where the two magnetization directions are parallel vs antiparallel. The transmission probability is in general higher when the two ferromagnets are magnetized parallel compared to antiparallel. Notably, the difference between the two configurations decreases as the CISS strength s increases. This is because with increasing s , electrons have a higher probability of encountering spin-flip reflections. This also explains why

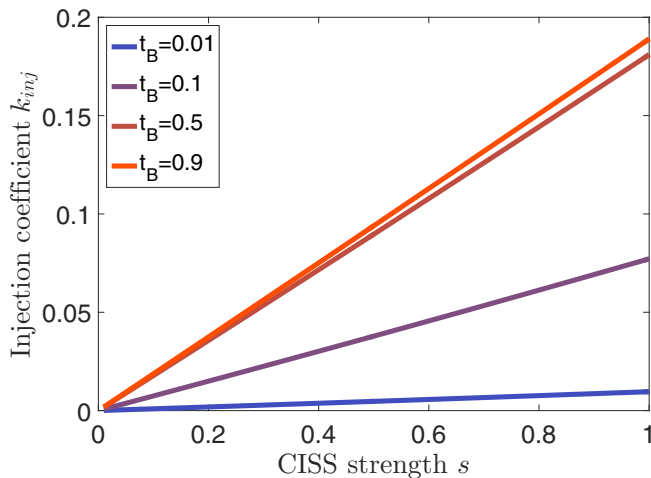


FIG. 16. Injection coefficient k_{inj} as a function of s (generalized CISS strength) for various t_B (contact barrier transmission), for the geometry described in Fig. 6(a) in the main text.

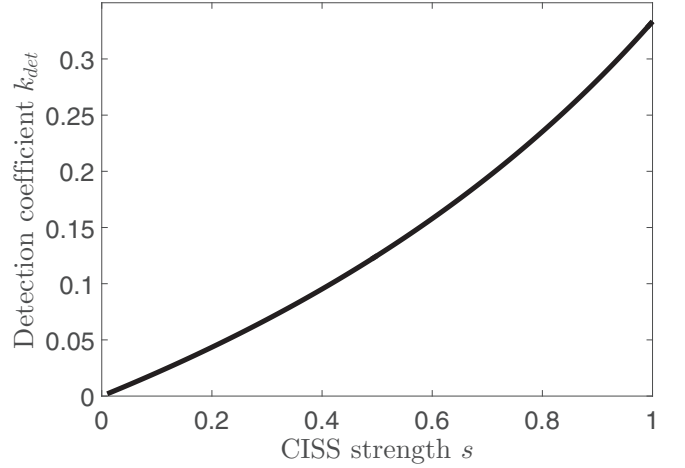


FIG. 17. Detection coefficient k_{det} as a function of s (generalized CISS strength) for the geometry described in Fig. 6(a) in the main text.

in a BCB model, where an ideal spin-flip process is present, switching the magnetization directions does not lead to any conductance variation. The direction of the current has no effect on the transmission and reflection probabilities, as is required by the linear regime.

For four-terminal geometries, we calculate here the spin injection and detection coefficients using the formulas derived in the main text, and we plot these coefficients as a function of the CISS strength s . Figure 16 shows the injection coefficient as a function of s for a few t_B values. Figure 17 shows the detection coefficient as a function of s , and Fig. 18 shows the ratio between four-terminal and two-terminal resistances as a function of s .

Last but not least, we discuss the spin-charge conversion property of the generalized CISS molecule. Substituting the corresponding transmission and reflection matrices into Eq. (B8), and solving the vector equation, we can obtain

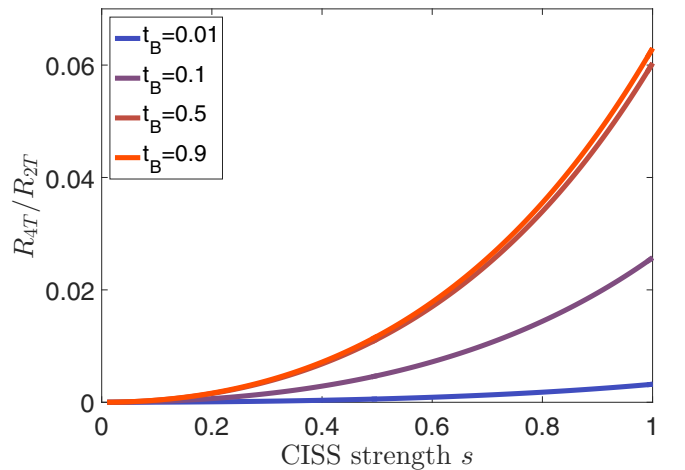


FIG. 18. The ratio between four-terminal and two-terminal resistances as a function of s (generalized CISS strength) for various t_B (contact barrier transmission), for the geometry described by Fig. 6(a) in the main text.

relations between the conversion coefficient k_{conv} and the chemical potential vector μ_A . Unlike the BCB model, here it

is not possible to drop out either μ_{nA} or μ_{sA} from the equation. The final result gives

$$k_{\text{conv}} = -\frac{\Delta\mu_n}{\Delta\mu_s} = \frac{(A - B - 1)s\mu_{nA} + \frac{1}{2}(b + B)s\mu_{sA}}{2(A + B - 1)s\mu_{nA} + (b + B)(-2 + 2A + 2B + s)\mu_{sA}}, \quad (\text{C10})$$

where a, b, A, B, s are the parameters in the transmission and reflection matrices of the generalized CISS model. This equation shows that a nonzero charge voltage difference ($\Delta\mu_n$) can give rise to a spin accumulation difference ($\Delta\mu_s$) across a generalized CISS molecule, and vice versa (spin-charge conversion). Interestingly, the conversion coefficient k_{conv} depends not only on the transmission and reflection matrices of the molecule, but also on the spin accumulation in the nodes connected to the molecule. If $s = 0$, i.e., the molecule does not exhibit any CISS effect, the spin-charge conversion property also diminishes ($k_{\text{conv}} = 0$).

With these discussions, we demonstrated that a generalized CISS molecule shows differences from the simplified BCB model. Nonetheless, these differences are rather quantitative than qualitative, and are not easily measurable in experiments. Furthermore, the generalized model also introduces extra degrees of freedom to calculations as it uses four variables to describe a CISS molecule, compared to one in the BCB model. Having taken the above into consideration, in the main text we only showed the results of the BCB model.

- [1] S. A. Wolf, D. D. Awschalom, R. A. Buhrman, J. M. Daughton, S. Von Molnar, M. L. Roukes, A. Yu. Chtchelkanova, and D. M. Treger, Spintronics: A spin-based electronics vision for the future, *Science* **294**, 1488 (2001).
- [2] R. Naaman and D. H. Waldeck, Chiral-induced spin selectivity effect, *J. Phys. Chem. Lett.* **3**, 2178 (2012).
- [3] R. Naaman and D. H. Waldeck, Spintronics and chirality: Spin selectivity in electron transport through chiral molecules, *Annu. Rev. Phys. Chem.* **66**, 263 (2015).
- [4] B. Göhler, V. Hamelbeck, T. Z. Markus, M. Kettner, G. F. Hanne, Z. Vager, R. Naaman, and H. Zacharias, Spin selectivity in electron transmission through self-assembled monolayers of double-stranded DNA, *Science* **331**, 894 (2011).
- [5] Z. Xie, T. Z. Markus, S. R. Cohen, Z. Vager, R. Gutierrez, and R. Naaman, Spin specific electron conduction through DNA oligomers, *Nano Lett.* **11**, 4652 (2011).
- [6] V. Kiran, S. P. Mathew, S. R. Cohen, I. Hernández Delgado, J. Lacour, and R. Naaman, Helicenes—a new class of organic spin filter, *Adv. Mater.* **28**, 1957 (2016).
- [7] M. Kettner, V. V. Maslyuk, D. Nürenberg, J. Seibel, R. Gutierrez, G. Cuniberti, K.-H. Ernst, and H. Zacharias, Chirality-dependent electron spin filtering by molecular monolayers of helicenes, *J. Phys. Chem. Lett.* **9**, 2025 (2018).
- [8] K. Ray, S. P. Ananthavel, D. H. Waldeck, and R. Naaman, Asymmetric scattering of polarized electrons by organized organic films of chiral molecules, *Science* **283**, 814 (1999).
- [9] I. Carmeli, V. Skakalova, R. Naaman, and Z. Vager, Magnetization of chiral monolayers of polypeptide: a possible source of magnetism in some biological membranes, *Angew. Chem., Int. Ed.* **41**, 761 (2002).
- [10] S. G. Ray, S. S. Daube, G. Leitus, Z. Vager, and R. Naaman, Chirality-Induced Spin-Selective Properties of Self-Assembled Monolayers of DNA on Gold, *Phys. Rev. Lett.* **96**, 036101 (2006).
- [11] D. Mishra, T. Z. Markus, R. Naaman, M. Kettner, B. Göhler, H. Zacharias, N. Friedman, M. Sheves, and C. Fontanesi, Spin-dependent electron transmission through bacteriorhodopsin embedded in purple membrane, *Proc. Natl. Acad. Sci. USA* **110**, 14872 (2013).
- [12] M. Á. Niño, I. A. Kowalik, F. J. Luque, D. Arvanitis, R. Miranda, and J. J. de Miguel, Enantiospecific spin polarization of electrons photoemitted through layers of homochiral organic molecules, *Adv. Mater.* **26**, 7474 (2014).
- [13] M. Kettner, B. Göhler, H. Zacharias, D. Mishra, V. Kiran, R. Naaman, C. Fontanesi, D. H. Waldeck, S. Sek, J. Pawłowski, *et al.*, Spin filtering in electron transport through chiral oligopeptides, *J. Phys. Chem. C* **119**, 14542 (2015).
- [14] K. Michaeli, V. Varade, R. Naaman, and D. H. Waldeck, A new approach towards spintronics—spintronics with no magnets, *J. Phys.: Condens. Matter* **29**, 103002 (2017).
- [15] O. B. Dor, S. Yochelis, S. P. Mathew, R. Naaman, and Y. Paltiel, A chiral-based magnetic memory device without a permanent magnet, *Nat. Commun.* **4**, 2256 (2013).
- [16] P. C. Mondal, N. Kantor-Uriel, S. P. Mathew, F. Tassinari, C. Fontanesi, and R. Naaman, Chiral conductive polymers as spin filters, *Adv. Mater.* **27**, 1924 (2015).
- [17] V. Varade, T. Markus, K. Vankayala, N. Friedman, M. Sheves, D. H. Waldeck, and R. Naaman, Bacteriorhodopsin based non-magnetic spin filters for biomolecular spintronics, *Phys. Chem. Chem. Phys.* **20**, 1091 (2018).
- [18] B. P. Bloom, V. Kiran, V. Varade, R. Naaman, and D. H. Waldeck, Spin selective charge transport through cysteine capped CdSe quantum dots, *Nano Lett.* **16**, 4583 (2016).
- [19] S. P. Mathew, P. C. Mondal, H. Moshe, Y. Mastai, and R. Naaman, Non-magnetic organic/inorganic spin injector at room temperature, *Appl. Phys. Lett.* **105**, 242408 (2014).
- [20] K. M. Alam and S. Pramanik, Spin filtering through single-wall carbon nanotubes functionalized with single-stranded DNA, *Adv. Funct. Mater.* **25**, 3210 (2015).
- [21] R. Gutierrez, E. Díaz, R. Naaman, and G. Cuniberti, Spin-selective transport through helical molecular systems, *Phys. Rev. B* **85**, 081404 (2012).

- [22] S. Yeganeh, M. A. Ratner, E. Medina, and V. Mujica, Chiral electron transport: scattering through helical potentials, *J. Chem. Phys.* **131**, 014707 (2009).
- [23] J. Gersten, K. Kaasbjerg, and A. Nitzan, Induced spin filtering in electron transmission through chiral molecular layers adsorbed on metals with strong spin-orbit coupling, *J. Chem. Phys.* **139**, 114111 (2013).
- [24] E. Medina, L. A. González-Arraga, D. Finkelstein-Shapiro, B. Berche, and V. Mujica, Continuum model for chiral induced spin selectivity in helical molecules, *J. Chem. Phys.* **142**, 194308 (2015).
- [25] K. Michaeli and R. Naaman, Origin of spin dependent tunneling through chiral molecules, [arXiv:1512.03435](https://arxiv.org/abs/1512.03435).
- [26] V. V. Maslyuk, R. Gutierrez, A. Dianat, V. Mujica, and G. Cuniberti, Enhanced magnetoresistance in chiral molecular junctions, *J. Phys. Chem. Lett.* **9**, 5453 (2018).
- [27] A.-M. Guo and Q.-f. Sun, Spin-Selective Transport of Electrons in DNA Double Helix, *Phys. Rev. Lett.* **108**, 218102 (2012).
- [28] A.-M. Guo and Q.-F. Sun, Spin-dependent electron transport in protein-like single-helical molecules, *Proc. Natl. Acad. Sci. USA* **111**, 11658 (2014).
- [29] T.-R. Pan, A.-M. Guo, and Q.-F. Sun, Spin-polarized electron transport through helicene molecular junctions, *Phys. Rev. B* **94**, 235448 (2016).
- [30] J. H. Bardarson, A proof of the Kramers degeneracy of transmission eigenvalues from antisymmetry of the scattering matrix, *J. Phys. A: Math. Theor.* **41**, 405203 (2008).
- [31] S. Matityahu, Y. Utsumi, A. Aharony, O. Entin-Wohlman, and C. A. Balseiro, Spin-dependent transport through a chiral molecule in the presence of spin-orbit interaction and nonunitary effects, *Phys. Rev. B* **93**, 075407 (2016).
- [32] S. Matityahu, A. Aharony, O. Entin-Wohlman, and C. A. Balseiro, Spin filtering in all-electrical three-terminal interferometers, *Phys. Rev. B* **95**, 085411 (2017).
- [33] A.-M. Guo, E. Díaz, C. Gaul, R. Gutierrez, F. Domínguez-Adame, G. Cuniberti, and Q.-f. Sun, Contact effects in spin transport along double-helical molecules, *Phys. Rev. B* **89**, 205434 (2014).
- [34] M. Büttiker, Role of quantum coherence in series resistors, *Phys. Rev. B* **33**, 3020 (1986).
- [35] M. Büttiker, Y. Imry, R. Landauer, and S. Pinhas, Generalized many-channel conductance formula with application to small rings, *Phys. Rev. B* **31**, 6207 (1985).
- [36] M. Büttiker, Four-Terminal Phase-Coherent Conductance, *Phys. Rev. Lett.* **57**, 1761 (1986).
- [37] M. Büttiker, Symmetry of electrical conduction, *IBM J. Res. Dev.* **32**, 317 (1988).
- [38] G. A. Prinz, Magnetoelectronics, *Science* **282**, 1660 (1998).
- [39] I. Adagideli, G. E. W. Bauer, and B. I. Halperin, Detection of Current-Induced Spins by Ferromagnetic Contacts, *Phys. Rev. Lett.* **97**, 256601 (2006).
- [40] F. J. Jedema, A. T. Filip, and B. J. van Wees, Electrical spin injection and accumulation at room temperature in an all-metal mesoscopic spin valve, *Nature (London)* **410**, 345 (2001).
- [41] M. Drögeler, C. Franzen, F. Volmer, T. Pohlmann, L. Banszerus, M. Wolter, K. Watanabe, T. Taniguchi, C. Stampfer, and B. Beschoten, Spin lifetimes exceeding 12 ns in graphene nonlocal spin valve devices, *Nano Lett.* **16**, 3533 (2016).
- [42] J. Ingla-Aynés, M. H. D. Guimarães, R. J. Meijerink, P. J. Zomer, and B. J. van Wees, 24- μm spin relaxation length in boron nitride encapsulated bilayer graphene, *Phys. Rev. B* **92**, 201410 (2015).
- [43] M. Gurram, S. Omar, S. Zihlmann, P. Makk, Q. C. Li, Y. F. Zhang, C. Schönenberger, and B. J. van Wees, Spin transport in two-layer-CVD-hBN/graphene/hBN heterostructures, *Phys. Rev. B* **97**, 045411 (2018).
- [44] D. Nürenberg and H. Zacharias, Spin-flip scattering in chiral induced spin selectivity using the Riccati equation, [arXiv:1808.00269](https://arxiv.org/abs/1808.00269).
- [45] L. Hu, H. Huang, Z. Wang, W. Jiang, X. Ni, Y. Zhou, V. Zielasek, M. G. Lagally, B. Huang, and F. Liu, Ubiquitous Spin-Orbit Coupling in A Screw Dislocation With High Spin Coherency, *Phys. Rev. Lett.* **121**, 066401 (2018).
- [46] See Supplemental Material at <http://link.aps.org/supplemental/10.1103/PhysRevB.99.024418>, where the transmission and reflection probabilities of each spin species are plotted as a function of t (BCB barrier transmission probability) for the FM-BCB and spin-valve geometries.